Adaptive Ultrasonic Imaging with the Total Focusing Method for Inspection of Complex Components Immersed in Water

L. Le Jeune*, S. Robert*, P. Dumas†, A. Membre† and C. Prada**

*CEA, LIST, Gif-sur-Yvette, F-91191, France
†IMASONIC, Voray-sur-l'Ognon, F-70190, France
**Institut Langevin, 1 rue Jussieu, 75238 Paris Cedex 05, France

Abstract. In this paper, we propose an ultrasonic adaptive imaging method based on the phased-array technology and the synthetic focusing algorithm Total Focusing Method (TFM). The general principle is to image the surface by applying the TFM algorithm in a semi-infinite water medium. Then, the reconstructed surface is taken into account to make a second TFM image inside the component. In the surface reconstruction step, the TFM algorithm has been optimized to decrease computation time and to limit noise in water. In the second step, the ultrasonic paths through the reconstructed surface are calculated by the Fermat's principle and an iterative algorithm, and the classical TFM is applied to obtain an image inside the component. This paper presents several results of TFM imaging in components of different geometries, and a result obtained with a new technology of probes equipped with a flexible wedge filled with water (manufactured by Imasonic).

INTRODUCTION

Non-contact ultrasonic inspections are mostly made in immersion in tanks where water acts as a coupling medium between the transducer and the inspected component. When the structure can not be totally immersed, a local immersion technique can be used such as a squirter or a new technology based on flexible wedge filled with water [1, 2]. Nevertheless, inspection of complex components can be problematic. Single element control is not feasible as ultrasonics beams are deflected and distorted by the complex surface. The phased-array technology allows to realize images under a complex surface thanks to the adjustment of the delay laws to the geometry under the probe. However, the geometry of the component as well as the position of the transducer have to be perfectly known, which is not usually the case.

To optimize the control of complex components in immersion, the idea is to develop adaptive methods allowing the measurement of the surface, then to adapt the delay laws to the real configuration of inspection. Several surface measurement techniques exist either based on the measurement of the times of flight between the array elements and the surface [3, 4] or the extraction of the surface geometry through the surface image, for example with the synthetic transmit aperture [5] (also called Total Focusing Method (TFM) in the NDT field). When the surface is extracted, the ultrasonic ray paths through the surface, and the associated times of flight, have to be calculated to produce an image inside the component. They can be found with different approaches. The most rigorous approach is to simulate the ultrasonic field radiated by a point in direction of the probe elements [6]. This allows a very accurate measurement of the times of flight but can not be embedded in portable systems. Most techniques are based on the Fermat's principle [7]. According to this principle, a wave follows the minimum time of flight path which can be determined by several methods (minimum travel time tree methods [8], function minimizing like the gradient descent method, roots finding such as the Newton-Raphson method).

The technique presented in this paper is based on the TFM imaging. The first part describes the two key-steps of the adaptive method: the surface measurement using an optimized TFM to reduce computation time and noise, and the determination of the ultrasonic paths . The second part presents experimental results obtained on different components with complex surface geometries immersed in a water tank. Also presented are local immersion results obtained thanks to a new transducer fitted with a flexible wedge filled with water.

PRINCIPLE OF THE ADAPTIVE IMAGING TECHNIQUE

The presented method is based on the TFM imaging. The principle is to make an image of the surface in order to determine its geometry. In this section, the principle and some optimizations of the TFM are presented. Next, an ultrasonic path computation method is presented in the second section.

Full Matrix Capture and Total Focusing Method

The Full Matrix Capture (FMC) consists in recording the all set of $N \times N$ signals $k_{ij}(t)$ (Fig. 1), where j $(1 < j < N)$ is a transmitter and i $(1 < i < N)$ is a receiver. The so called $K(t)$ matrix thus obtained is the basis of several post-processing techniques as the synthetic imaging TFM which allows to focus, in emission and reception, on all points of an image area. This method is applied to the analytic time-domain signals $(S_{ij}(t))$ obtained by the Hilbert's transform of the $k_{ij}(t)$ signals:

$$S_{ij}(t) = k_{ij}(t) + jh[k_{ij}(t)]. \tag{1}$$

Considering a point P in a TFM image, the amplitude $A(P)$ at this point is given by:

$$A(P) = |\sum_{i=1}^{N} \sum_{j=1}^{N} W_i^p W_j^p S_{ij}(t_{ij}^P = t_i^P + t_j^P)|, \tag{2}$$

where t_i^P (resp. t_j^P) is the time of flight between receiver i (resp. transmitter j) and point P, and W_i^p (resp. W_j^P) is a weighting factor in reception (resp. in transmission).
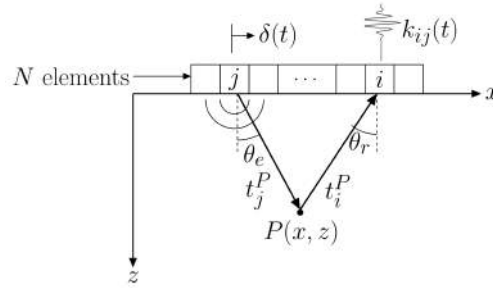

FIGURE 1. Inter-element impulse response $k_{ij}(t)$ for a N elements transducer.

The TFM imaging provides better image resolution than any other standard imaging technique (focused Bscan, Sscan,...): the spatial resolution is optimized at any depth, and a single FMC acquisition can be used to measure the surface and build an image inside the component. Its main drawback is the computation time it may require if the number of elements or focusing points is high.

Surface Measurement with TFM Imaging

A complex steel mock-up representative of a "leveled weld" surface is used to illustrate the surface measurement method (Fig. 2). The transducer is a $N = 128$ elements probe (pitch $d = 0.8$ mm) with a central frequency of 2 MHz. The reconstruction zone ($\square$) under the probe has the following dimensions: $L_x = 102$ mm, $L_y = 10$ mm. It has been discretized in $n_x = 200$, $n_y = 200$ pixels.

In the classical TFM method, there are $N \times N \times n_x \times n_y$ ($128 \times 128 \times 200 \times 200$) summations of signals $k_{ij}(t)$. Thus, the main goal is to reduce the computation time by decreasing the number of signals to process. To this end, we consider that above a certain distance between a transmitter and a receiver, the signal does not bring a significant contribution and that it should not be taken into account.

To determine what are the significant $k_{ij}(t)$, an amplitude threshold is defined for each emission. For an emission j, the maximum amplitude $max_i|k_{ij}(t)|$ is measured among N signals. The threshold is fixed in function of this maximum (for example, at -12 dB):

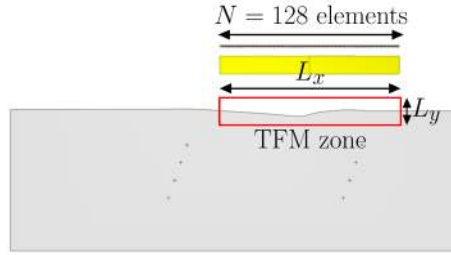$$\text{Threshold}_j = \frac{max_i|k_{ij}(t)|}{4} \tag{3}$$

FIGURE 2. Geometry of a leveled weld surface and probe position.

Only the $k_{ij}(t)$ signal having a maximum amplitude above the threshold are recorded. The amplitude threshold has to be variable because the surface complexity leads to large variations of the signal amplitudes depending on the emission. Taking the same threshold for all transmissions might eliminate too many signals. Figure 3 shows two examples of the elements of $K(t)$ that are kept with a $-12\,\text{dB}$ threshold.
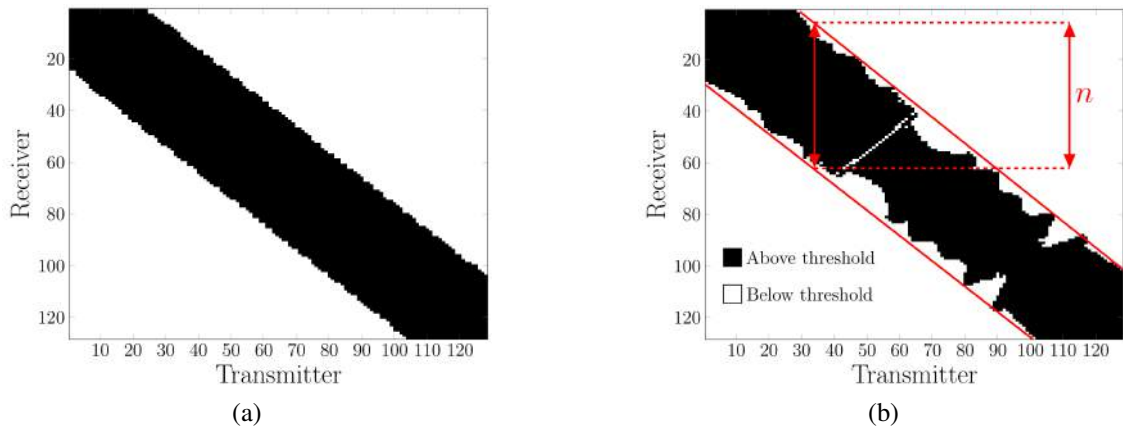

FIGURE 3. $K(t)$ matrix representation after thresholding. (a) flat surface, (b) complex surface.

Figures 3a and 3b are obtained for a flat and a complex surface, respectively. The white and black pixels represent the $k_{ij}(t)$ that are under or above the threshold. The ordinates (resp. abscissa) axis represents the receiver (resp. transmitter) number. A significant amount of the $k_{ij}(t)$ (approximatly 68 %) is not taken into account, resulting in a reduction of the number of operations as. Figure 3 shows that the significant $k_{ij}(t)$ are in a zone around the diagonal of the matrix. The width n of the zone gives the number of elements to keep in reception. For the configuration described in Fig. 2, at most 52 adjacent elements are kept in reception for each emission j. A TFM zone is defined under the sub-aperture ($L'_x = n \times d$). This zone contains n'_x computation points along the x axis. To obtain the complete image of the surface, the sub-aperture is moved along the probe with a step of one element (Fig. 4).
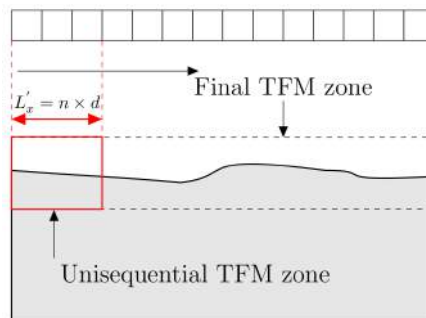

FIGURE 4. Moving TFM principle.

A partial image associated with an emission j is computed as follows:

$$A_j(P) = \sum_{i=j-\frac{n}{2}}^{j+\frac{n}{2}} W_i^p W_j^p S_{ij}(t_{ij}^P),$$

(4)

with $S_{ij}(t_{ij}^P) = 0$ if $j - \frac{n}{2} < 1$ or $j + \frac{n}{2} > N$. The weighting factors W_j^p (resp. W_i^p) are the element directivity functions in transmission (resp. in reception). The elements are assumed to be identical having the directivity function in transmission as in reception given by [9]:

$$W_j^p(\theta_p) = \frac{\sin\left(k\frac{a}{2}\sin\theta_j^P\right)}{k\frac{a}{2}\sin\theta_j^P}\cos\theta_j^P,$$

(5)

with a the width of an element and θ_j^p the observation angle between, the element j and the computation point P. Then the final image is obtained by summing all the partial images:

$$A_{tot}(P) = |\sum_{j=1}^{N} A_j(P)|.$$

(6)

With the moving TFM principle, the whole image is obtained with $N \times n \times n_x' \times n_y$ ($128 \times 52 \times 108 \times 200$) summations. Thus, the number of operations is divided by 5 compared to the "classical" TFM. Figure 5 presents the results obtained with the classical TFM (Fig. 5a) and with the moving TFM (Fig. 5b).
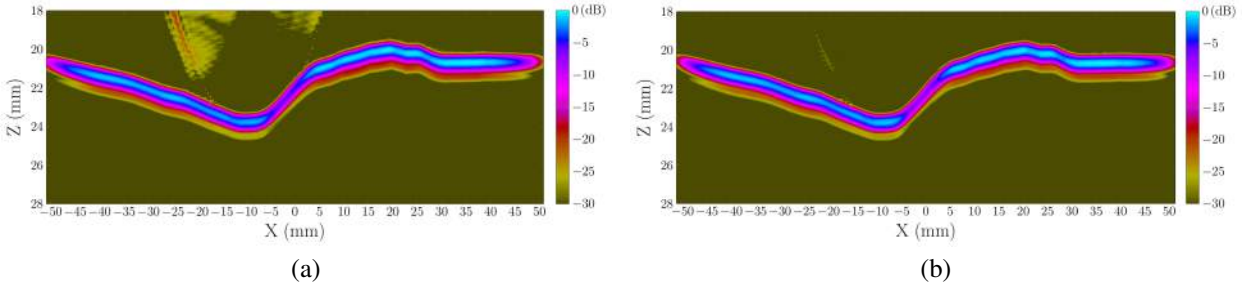

FIGURE 5.   Surface imaging by TFM. (a) classical method, (b) moving TFM.

It shows that the two images are very similar. In the moving TFM case, we note a reduction of the noise amplitude in the water due to the weighting of the signals by the element directivity function. Then the profile is extracted by detecting the maximum echo envelop on each column of the image, and a moving average is used to smooth the profile. Figure 6a shows the profiles obtained with the classical TFM (+) and the moving TFM (x) compared to the real profile (O) given by the manufacturer.
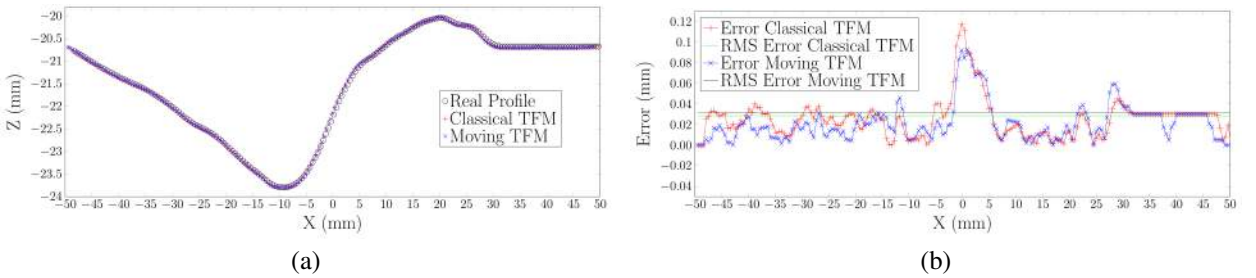

FIGURE 6.   Surface measurement. (a) classical TFM (+), moving TFM (x), real (O) profiles, (b) Errors and RMS errors between real and extracted profiles by classical TFM (+), moving TFM (x).

The two measured profiles agree very well with the real one. Figure 6b shows that the root mean square (RMS) errors between the real and the extracted profiles are less than 0.04 mm. The moving TFM allows a surface measurement as good as the classical TFM but reduce the time of computation.

Ultrasonic Path Computation

After the surface measurement, the classical TFM is applied a second time to make an image under the surface. To this end, the times of flight t_j^P between the elements and the points P of the image area under the surface (Fig. 7), have to be computed. The determination of these times of flight should use the profile extracted previously while minimizing the computation time.
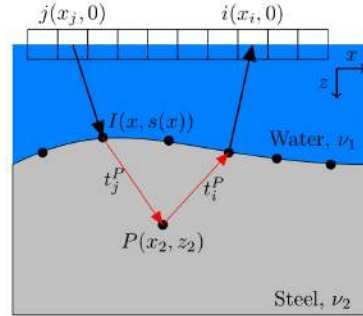

FIGURE 7. Ultrasonic path between transmitter j and receiver i.

The time of flight between an element and the calculation point P passing by the surface $s(x)$ is given by:

$$t_j^P(x) = \frac{\sqrt{(x-x_j)^2 + s(x)^2}}{v_1} + \frac{\sqrt{(x_2-x)^2 + (z_2 - s(x))^2}}{v_2}, \qquad (7)$$

where v_1 and v_2 are the sound velocities in the water and in the inspected material. The Fermat's principle states that the physical path corresponds to the minimum time of flight. The starting and arriving points being known, only the coordinates of the impact point I on the surface have to be determined. For a pair element/computation point, the estimation of the impact point, obtained by using the iterative method of the gradient descent, is given by:

$$x^{(k+1)} = x^{(k)} - \frac{t'(x^{(k)})}{t''(x^{(k)})}, \qquad (8)$$

where k is the number of the iteration. As $v_2 \approx 3v_1$, the impact point I is close to the element, thus the initialization value $x^{(0)}$ is taken at the abscissa of the element. The first and second derivatives are calculated by finite differences.
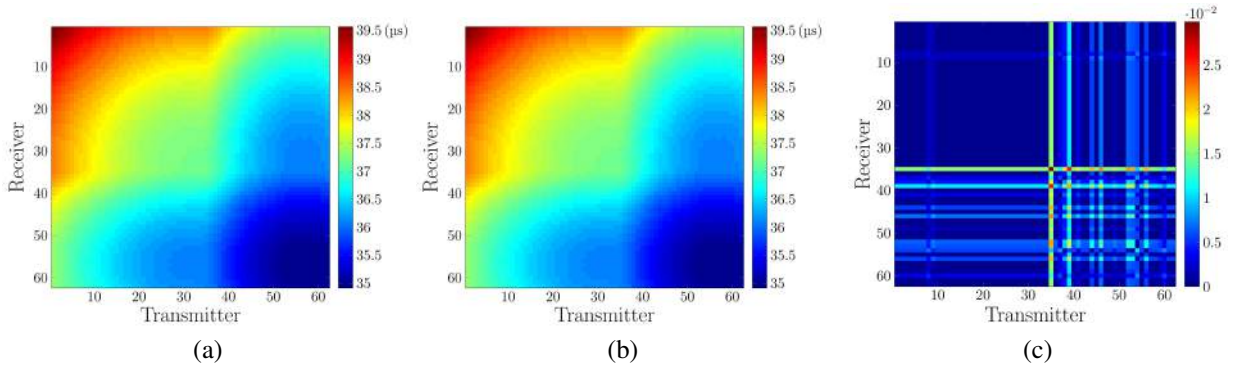

(a)

(b)

(c)

FIGURE 8. Time of flight computation. (a) times of flight t_{ij}^P (Eq. 2) for each couple transmitter/receiver for $k = 2$, (b) times of flight t_{ij}^P (Eq. 2) for each couple transmitter/receiver for $k = 100$, (c) normalized time of flight difference between the two matrices.

Figures 8a and 8b represent the times of flight t_{ij}^P (Eq. 2) calculated for $k = 2$ and $k = 100$ for a point under the surface in the configuration described by Fig. 2 with a 64 elements transducer. Figure 8c shows the normalized difference ($c\Delta t_{ij}^P/\lambda$, c: ultrasound velocity in the component, Δt_{ij}^P: difference of the times of flight matrices, λ: wavelength in the component) between two matrices calculated for two iterations values ($k = 2$ and $k = 100$). The subtraction of the two matrices after normalization gives a maximum difference of approximately 0.03 . Hence, two to three iterations are enough to find the coordinates of the impact point I.

EXPERIMENTAL RESULTS

Immersion in a Water Tank

The adaptive algorithm has been tested on three components with different geometries:

- Leveled weld (irregular geometry).
- Weld bead (convex geometry).
- Nozzle (concave geometry).

A 64 elements transducer with 0.8 mm pitch and a central frequency of 2 MHz is used. In the three configurations, the amplitude threshold is fixed at -6 dB for each emission. This threshold has been chosen to reduce as much as possible the number of operations to process, while keeping a reconstruction quality close to the classical TFM. The image area is 200×200 pixels.

The leveled weld (Fig. 9a) is a steel block of 256 mm $\times$ 80 mm. It contains 4 side drilled holes (SDH) of 2 mm diameter, located under the complex part of the surface and at a depth between 19 mm to 49 mm (with respect to the flat part). Figure 9b shows that 68 % of the $k_{ij}(t)$ are eliminated and that $n = 32$ elements are needed in reception.
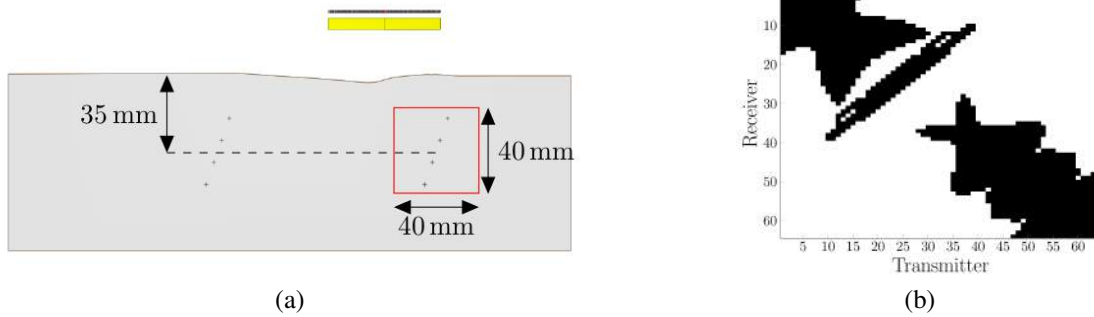

(a)

(b)

FIGURE 9. Leveled weld. (a) specimen geometry, (b) $K(t)$ matrix with a threshold at -6 dB.

The weld bead (Fig. 10a) is a stainless steel mock-up of 255 mm $\times$ 40 mm. It contains 5 SDH of 2 mm diameter at a depth of 30 mm, spaced by 25 mm. For this case, the $K(t)$ matrix (Fig. 10b) shows that 64 % of the $k_{ij}(t)$ are eliminated and that $n = 30$ elements are needed to reconstruct the profile.

(a)

(b)

FIGURE 10. Weld bead. (a) specimen geometry, (b) $K(t)$ matrix with a threshold at -6 dB.

The nozzle (Fig. 11a) is in steel and its dimensions are 190 mm $\times$ 50 mm. The 5 SDH are separated by 10 mm in depth and 5 mm laterally. Figure 11b shows that 50 % of the $k_{ij}(t)$ are eliminated. The zone along the diagonal includes $n = 40$ elements. In this case, the probe has to be tilted to prevent it from tripping over the edge of the component.
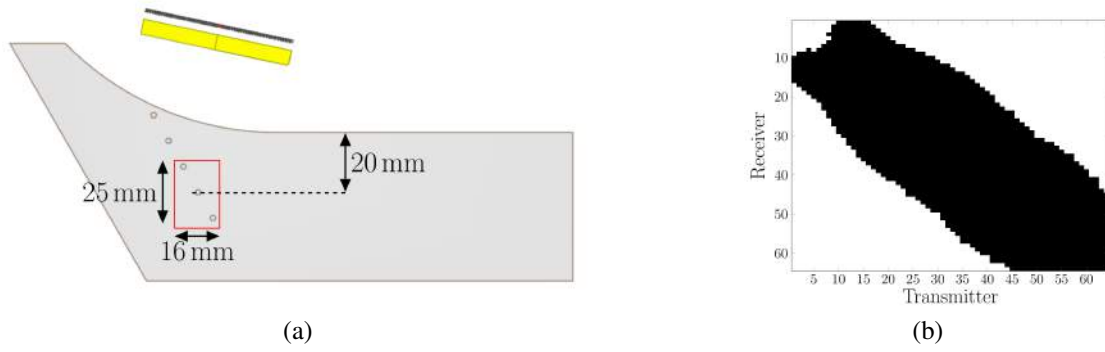
(a)

(b)

FIGURE 11. Nozzle. (a) specimen geometry, (b) $K(t)$ matrix with a threshold at $-6\,\mathrm{dB}$.

In each case, the images under the surface have been computed by taking into account the real profile (manufacturer) and by applying the adaptive method. Figure 12 shows that the adaptive method gives results similar to those obtained with the real profile. The positions of the SDH echoes in the images are identical for each setup and the signal to noise ratio (SNR) is approximately the same ($\pm 2\,\mathrm{dB}$).
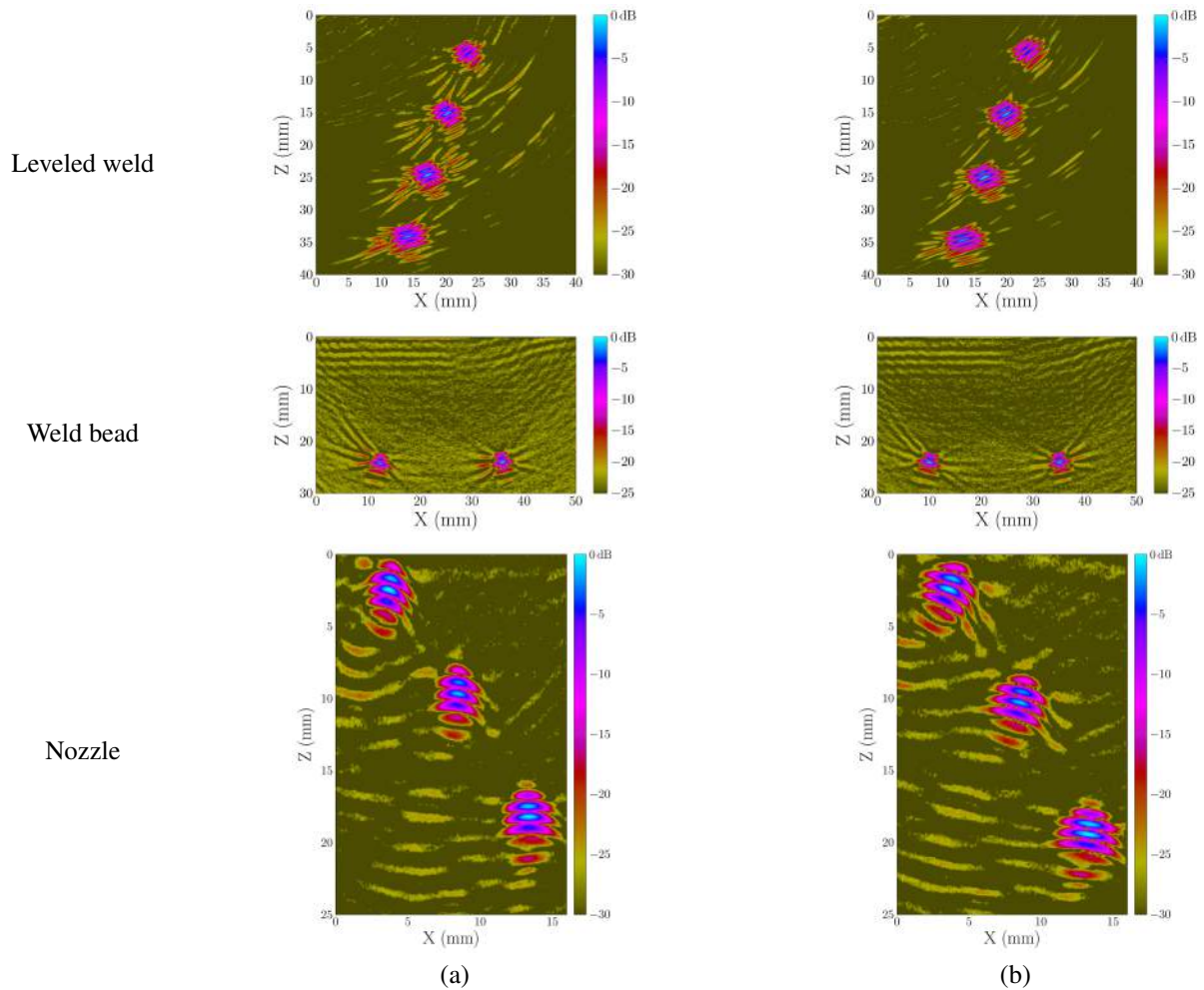
Leveled weld

Weld bead

Nozzle

(a)

(b)

FIGURE 12. TFM images under the surface. (a) adaptive method, (b) real profile.

Instrumentation of a New Transducer Fitted with a Flexible Wedge Filled with Water

In an industrial context, total immersion control (in tank) is not always possible, like for on-site inspection. To overcome this problem, Imasonic develops a new technology for "local immersion" control that consists in a transducer attached to a flexible wedge filled with water (Fig. 13).
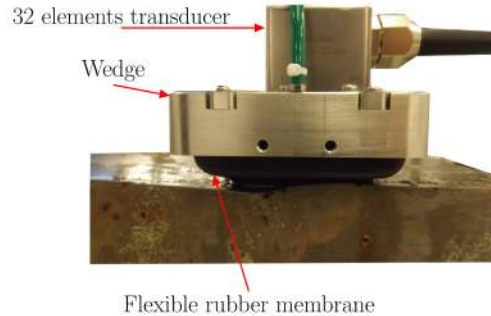

FIGURE 13. Transducer equipped with a flexible wedge.

The adaptive method has been tested with this kind of probe on the leveled weld configuration (Fig. 14a). The transducer has 32 elements (pitch 0.6 mm) and radiates at a central frequency of 5 MHz.
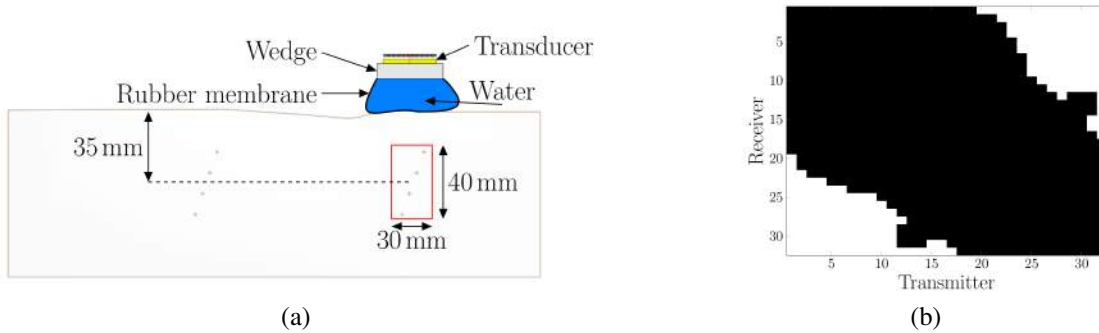

FIGURE 14. Flexible wedge. (a) control setup, (b) $K(t)$ matrix with a threshold at -6 dB.

Figure 14b shows that approximately 20 % of the k_{ij} signals are eliminated. This case points out that for arrays with few elements, the moving TFM is not really effective.

The results obtained with the adaptive method and the real profile can be compared in Fig. 15. The two methods give similar results with SDH echoes located at the same positions and equivalent SNR (± 2 dB).
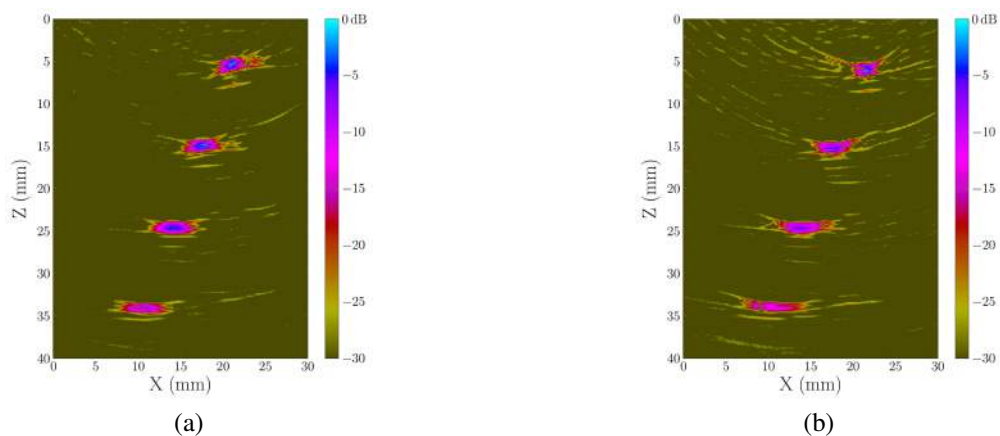

FIGURE 15. TFM images. (a) adaptive method, (b) real profile.

The adaptive algorithm presented and illustrated above has been implemented in an embedded system manufactured by M2M. The portable system, called Gekko, is a 64 parallel channels allowing several types of ultrasonic inspections.
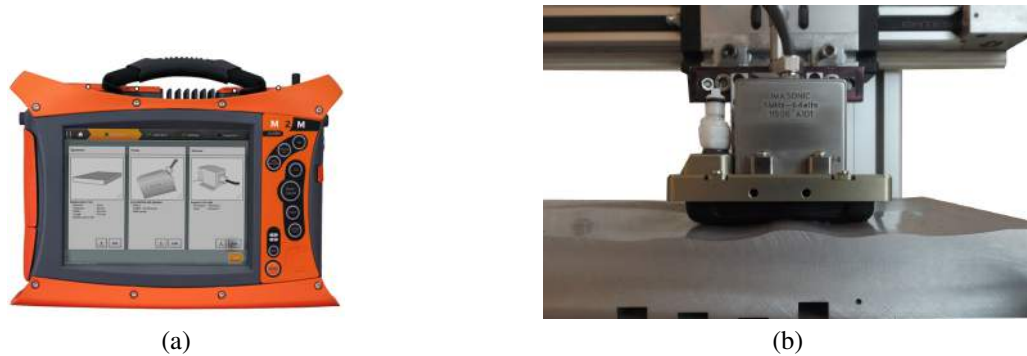

<table>
<tr><td>(a)</td><td>(b)</td></tr>
</table>

FIGURE 16. Control setup. (a) Gekko ultrasonic system, (b) transducer fitted with a flexible wedge and inspected mock-up.

The control setup comprises the Gekko system (Fig. 16a) coupled with a 64 elements probe at 5 MHz fitted with a flexible wedge (Fig. 16b). The component inspected is an aluminum mock-up including notches of 10 mm thickness with different depths (1 mm, 3 mm, 5 mm and 6 mm) representatives of corrosion and two SDH of 2 mm diameter (Fig. 16b). The same defect pattern is located under the flat surface and the complex one.
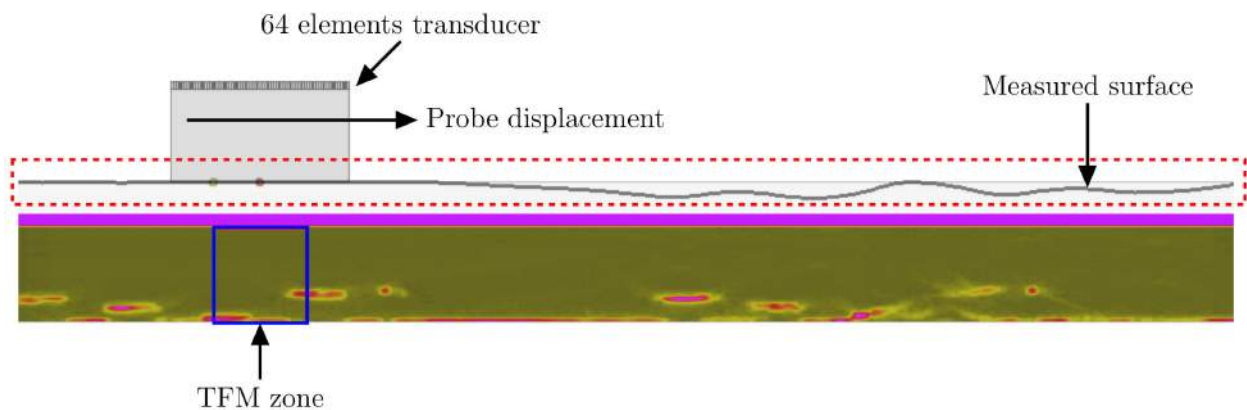

FIGURE 17. Real-time adaptive TFM with a mechanical displacement.

Figure 17 shows the results of an adaptive TFM acquisition obtained with the flexible wedge transducer connected to the Gekko system. The surface measurement and the TFM image are performed under the probe aperture and the final image is obtained by following the same moving TFM principle than in the previous section, but the electronic scan is replaced by a mechanical one. Approximately 10 fps can be reached in this mode.

CONCLUSIONS AND PERSPECTIVES

In this paper, we have presented an adaptive method based on the TFM, allowing to make images under a complex surface in total or local immersion. First, the unknown surface geometry is measured through an optimized TFM that reduces both the computation time and the noise in the image. Then, the extracted profile is used to compute the ultrasonic paths through the surface and, then, to make an image in the material. The results obtained with the adaptive method have been compared to the theoretical ones (i.e. the theoretical profil is taken into account in the TFM processing). They have shown that the adaptive method gives good results and is robust whatever the geometry (convex, concave, irregular). Finally, the algorithm has been tested with a new type of probe equipped with a flexible

wedge filled with water allowing to perform local immersion testing. The real-time processing has been embedded in the Gekko ultrasonic system, commercialized by M2M.

The perspectives of this work are the use of multi-modal imaging (half-skip mode, mode conversion) and the generalization of the method to 3-Dimensional imaging.

REFERENCES

1. C. Bird, and I. Pettigrew, "Qualification of a Phased Array Inspection of Thin Welds," in *18th World Conference on Nondestructive Testing*, 2012, vol. 9.
2. J. Russell, R. Long, and P. Cawley, *American Institute of Physics Conference Series* **1211**, 831–838 (2010).
3. J. Camacho, J. Cruza, J. Brizuela, and C. Fritsch, *Ultrasonics, Ferroelectrics, and Frequency Control, IEEE Transactions on* **61**, 673–684 (2014).
4. T. Sakamoto, and T. Sato, *IEICE Transactions on Communications* **E87-B**, 1357–1365 (2004).
5. R. Chiao, L. Thomas, and S. Silverstein, "Sparse array imaging with spatially-encoded transmits," in *Ultrasonics Symposium, 1997. Proceedings., 1997 IEEE*, 1997, vol. 2, pp. 1679–1682.
6. P. Calmon, A. Lhemery, and L. Paradis, "Modeling of ultrasonic fields and their interaction with defects," in *Ultrasonics Symposium, 1998. Proceedings., 1998 IEEE*, 1998, vol. 1, pp. 779–783.
7. M. Parrilla, J. Brizuela, J. Camacho, A. Ibaez, P. Nevado, and C. Fritsch, "Dynamic focusing through arbitrary geometry interfaces," in *Ultrasonics Symposium, 2008. IUS 2008. IEEE*, 2008, pp. 1195–1198.
8. A. Zhao, Z. Zhang, and J. Teng, *Journal of Geophysics and Engineering* **1**, 245–251 (2004).
9. A. R. Selfridge, G. S. Kino, and B. T. Khuri-Yakub, *Applied Physics Letters* **37**, 35–36 (1980).